

Journal of Applied Remote Sensing

RemoteSensing.SPIEDigitalLibrary.org

Geometry of statistical target detection

William F. Basener
Brian Allen
Kristen Bretney

SPIE.

William F. Basener, Brian Allen, Kristen Bretney, "Geometry of statistical target detection," *J. Appl. Remote Sens.* **11**(1), 015012 (2017), doi: 10.1117/1.JRS.11.015012.

Geometry of statistical target detection

William F. Basener,^{a,*} Brian Allen,^b and Kristen Bretney^c

^aRochester Institute of Technology, The School of Mathematical Sciences,
Rochester, New York, United States

^bMessiah College, Department of Mathematics, Mechanicsburg, Pennsylvania, United States

^cLoyola Marymount University, Department of Mathematics, Los Angeles,
California, United States

Abstract. This paper presents an investigation into the underlying geometry and performance of various statistical target detection algorithms for hyperspectral imagery, presents results from algorithm testing, and investigates general trends and observable principles for understanding performance. Over the variety of detection algorithms, there is no universally best performing algorithm. In our test, often top performing algorithms on one class of targets obtain mediocre results on another class of targets. However, there are two clear trends: quadratic detectors such as ACE generally performed better than linear ones especially for subpixel targets (our top 15 scoring algorithms were quadratic detectors), and using anomaly detection to prescreen image spectra improved the performance of the quadratic detectors (8 of our top 9 scoring algorithms using anomaly prescreening). We also demonstrate that simple combinations of detection algorithms can outperform single algorithms in practice. In our derivation of detection algorithms, we provide exposition on the underlying mathematical geometry of the algorithms. That geometry is then used to investigate differences in algorithm performance. Tests are conducted using imagery and targets freely available online. The imagery was acquired over Cooke City, Montana, a small town near Yellowstone National Park, using the HyMap V/NIR/SWIR sensor with 126 spectral bands. There are three vehicle and four fabric targets located in the town and surrounding area. © 2017 Society of Photo-Optical Instrumentation Engineers (SPIE) [DOI: [10.1117/1.JRS.11.015012](https://doi.org/10.1117/1.JRS.11.015012)]

Keywords: hyperspectral; target detection; adaptive coherence/cosine estimator; matched filter; topological anomaly detection.

Paper 16659 received Sep. 5, 2016; accepted for publication Jan. 26, 2017; published online Feb. 21, 2017.

1 Introduction

Target detection in hyperspectral imagery is the detection of known target spectra within pixel spectra from a hyperspectral image. The underlying model for the creation of the hyperspectral image involves photons traveling from an illumination source, typically the sun, through the atmosphere, reflecting off objects, and then traveling through the atmosphere again to the sensor. Usually, an atmospheric compensation (or correction) process is applied to put the image in units of percent reflectance for each wavelength. For longwave hyperspectral imagery the measurement is of emitted photons, but we restrict to the reflectance case for simplicity of discussion.

Because the target object may occupy only a subset of the region covered by a pixel, there can be photons from material surrounding the target object that are measured by the sensor in the same pixel at the target. Other physical phenomena, such as multiple scattering effects, dirt on the target object, targets beneath trees, and ground that can be seen through a fabric target will also create photons that enter the sensor at the pixel location that did not simply reflect off of the target. The simplifying model for the resulting spectra is that a pixel over a target will be a linear combination of target spectra and background spectra

*Address all correspondence to: William F. Basener, E-mail: wfbmsa@rit.edu

$$\mathbf{x} = \alpha \mathbf{b} + \beta \mathbf{t} + \varepsilon, \quad (1)$$

where \mathbf{x} is the pixel spectrum, \mathbf{b} is a background spectrum, \mathbf{t} is target spectrum, ε is error/noise, and α and β are constants. The target and pixel spectra are vectors whose length is the number of bands in the image. In the case in which the target is subpixel, it can be assumed that either $\alpha = 1$ and $\beta < 1$, called the additive model, or that $\alpha + \beta = 1$ which is called the replacement model. If the target is assumed to be full pixel, then $\alpha = 0$ and $\beta = 1$. There are a number of target detection algorithms that have been developed based on different methods for modeling the target and background classes and how they combine in a resulting target pixel. The focus of this paper is algorithms that use a probability distribution to model the target and background classes. A complete exposition of hyperspectral image collection and the detection process can be found in Refs. 1 and 2.

The goal of this paper is to explore the geometry that results from the formulas for some of the more common detection algorithms and variants, conduct tests using data with multiple targets to observe the geometry and its effects on detection accuracy, and from that develop general observations and guidelines for choosing a detection algorithm. We should not expect to find a single detection algorithm that will be the best performer in all circumstances; there is sufficient variation among images, targets, confusers (nontarget materials that are similar to the target), and phenomenology that any reasonable detection algorithm will perform well on occasion. What we do find are general principles about strengths and weaknesses of different classes of algorithms and some trends in performance. These general principles come from both the assumptions that go into the derivation of the algorithm and the resulting geometry. We hope that these general principles will be helpful in understanding the “personality” of different detectors, in choosing a reliable detection algorithm for a given purpose, and for guiding development for future work.

In Sec. 2, we present an overview of target detection algorithms and related formulas. In Sec. 3, we provide the formulas for a number of statistical detection algorithms and the underlying geometry. We provide test results in Sec. 4 along with plots showing the geometry of the separation surfaces in our test data. Conclusions and general principles are presented in Sec. 5.

For our test, we use hyperspectral data available online.³ The imagery was acquired on July 4, 2006 over Cooke City, Montana, a small town near Yellowstone National Park, using the HyMap V/NIR/SWIR sensor with 126 spectral bands. The ground sample distance (distance between the centers of adjacent pixels measured on the ground) is ~ 3 m. There are four fabric targets (red cotton, yellow cotton, blue cotton, and red nylon) and three vehicles (green SUV, white Toyota T100, and a red Subaru), all of which are subpixel targets, located in the town and surrounding area. Each fabric has a 2 m square target, and the blue cotton and red nylon each has an additional smaller 1 m square target. The white T100 target is provided as a spectra taken from the white vehicle body and a spectra from the black truck bed. A description of the collection is given in Ref. 4.

2 Target Detection Fundamentals

In this section, we introduce the fundamental mathematics of target detection, including a derivation of a detection algorithm. The concepts from this section will be used in Sec. 2 to determine the geometry of detection algorithms.

For a number of target detection algorithms and variants, we present the assumptions that are made in deriving the algorithm as well as the resulting geometry of how the algorithm separates targets from background. We present the assumptions that are made in deriving the algorithm as well as the the resulting geometry of how the algorithm separates targets from background.

Target detection algorithms in hyperspectral can be separated at a high level into two categories: algorithms that model the variation in classes and those that directly compare the target spectrum and pixel spectra. While not the focus of this paper, direct measurement methods are useful for full-pixel cases, particularly with common materials. We do not pose a rigorous definition of common, although as a functional definition we could say common materials are those sufficiently common in an image that they are not readily separable from background. For example, detection of vegetation types, roads, soils, or rooftops in a populated area would be common materials.

The most common direct comparison detection algorithm is spectral angle mapper (SAM), which measures the angle between the test pixel and the target spectra, treating the spectra as vectors based at the origin. A small angle indicates a pixel that is likely to contain a target. SAM is invariant with respect to pixel and target intensity. That is, $\text{SAM}(\alpha \mathbf{x}) = \text{SAM}(\mathbf{x})$ for any vector \mathbf{x} and scalar α . This means that the SAM is forgiving of illumination variation or imperfections in atmospheric estimation of an overall gain, although neither of these factors is a simple scalar multiplication. A target in direct sunlight will be brighter than one in partial shade, but the one in shade will be illuminated with light of different wavelengths from the sky rather than directly from the sun. The other direct comparison method worth mentioning is correlation, computed using Pearson's correlation coefficient, $R^2 = (\mathbf{x} - \mu_x)(\mathbf{t} - \mu_t) / (\sigma_x \sigma_t)$, where \mathbf{x} is the pixel spectrum vector, μ_x is the mean of the values in the pixel vector, \mathbf{t} is the target spectrum vector, μ_t is the mean of the values in the target vector, and σ_x and σ_t are the standard deviations of the pixel and target spectra vectors. Note that the means here are scalars, being the mean value of a single spectrum, and the subtraction in the numerator means we subtract the scalar value from each component in the vector. Elsewhere in this paper, a mean will be the mean spectrum of a class of spectra. The correlation is invariant with respect to gain (multiplying all values in the spectra by a scalar) and offset (adding a scalar to all values in the spectrum).

Target detection methods that model the background can be further separated into the ones that use endmembers (which are either known material spectra or pixel spectra from the image) with linear mixing to measure the presence of target mixed with background (see Refs. 5–7), and those that use a statistical model of the background. While the linear mixture methods are not necessarily less accurate than statistical methods, the linear mixture methods are less common in practice partially because they appear less robust, relying on selection of individual spectra for the background model. For more on linear mixture detection methods, see Ref. 7. A practical implementation of linear mixing detection, combined with statistical detection, is given in Ref. 8. In that implementation, statistical target detection is used as a first stage to determine pixels that may be targets. A second stage process determines endmembers in a local window around each of the detected pixels (excluding detected pixels from being endmembers) and uses stepwise regression linear unmixing of the pixel against the target and endmembers. Consequently, the endmembers used are likely local background for the target and not targets or confuser pixels. The results from the statistical and linear unmixing methods are output. This procedure is used in Ref. 9, where the unmixing and an identification step are done using Bayesian model averaging regression.

Statistical target detection algorithms, which are the focus of this paper, model the variation in the background and target spectra with probability density functions. These functions are computed via mean and covariance or correlation matrices and then identify pixels that are more like the target and less like the background. Informally, the detector should suppress background signal while amplifying the target. From a statistical Bayesian approach, these detectors are derived as likelihood ratio tests given the probability that a test pixel contains a target divided by the probability that the pixel does not contain a target.

We first provide a derivation from likelihoods for the full pixel case in Sec. 2.1. Because the statistical derivations have been provided elsewhere (See Refs. 1 and 2), we do not provide additional derivations. In Sec. 2.2 we provide the underlying mathematics of principle components and whitening, which is useful for understanding the geometry and for efficient software implementation. In Sec. 3, we provide an explanation of the underlying geometry and mathematics for statistical target detection for several standard detection algorithms and a few variants.

2.1 Target Detection as a Likelihood Test with Full Pixel Assumptions

An image pixel on a material will not have a spectrum that is a perfect match to a library-measured spectrum for that material. There are many reasons for this difference. There is intrinsic variation with samples of a material; spectra from a plant species will vary depending on the amount of constituents (chlorophyll, cellulose, etc.) in the plant, which in turn varies with the age, health, and season of the plant. Man-made materials vary depending on the manufacturing and wear, but tend to be more consistent than natural ones. There is also variation from image

collection, depending on atmospheric variation, illumination, and related factors. There is also inherent noise in the collection; hyperspectral sensors typically have a high signal-to-noise ratio, but are susceptible to individual bad detectors on the focal plane. All of these factors are modeled collectively by assuming that there is an underlying probability distribution for the spectrum that will be observed for a material, and that this distribution is multivariate normal. For the purpose of target detection, the (unrealistic but useful) assumption is also made that the image consists of two classes: a target class for pixels on the target material and a background class of everything else, each of which can be modeled as a multivariate normal distribution. While the assumption that the background of an image can be modeled by a single multivariate normal distribution is possibly the most clearly violated assumption, there does not seem to be a simple best alternative, a topic we discuss in Sec. 5.

To derive a detection formula for a full pixel target, assume that the image consists of non-target pixels and target pixels, that the background and target are each modeled by a multivariate normal distribution, that the covariances for the distributions are equal, that the background class has mean μ , and the target class has mean \mathbf{t} . These are the assumptions made when deriving the standard matched filter.

The target class mean is a measured spectrum from the target material, from a lab instrument, a field instrument, or from image pixels. The standard estimation of the covariance for the background is done by computing the covariance matrix (see Sec. 2.2) from all pixels in the image, although there are important variations. If a region within the image is known to be free of target, the covariance can be estimated using just pixels in this region (see Ref. 1). The covariance can be computed from nonanomalous pixels as determined by an anomaly detection method, as we describe in Sec. 3.5. The covariance for the target class is usually assumed to be the same as for the background, in part for convenience because there is rarely sufficient pixels to compute a proper target covariance. The background mean is most often computed as the mean of all pixels used to compute the covariance, which provides the expected value for the mean and covariance of the background class. Computing the mean from the full image (or a large portion of it) is referred to as global statistics.

In contrast to global statistics, local statistics estimation involves computing the mean and/or covariance from a region surrounding the test pixel. In practice, to get a sufficient number of pixels for a robust covariance and to manage computational time, the covariance is estimated using a global method. Computing a local mean for the background, typically using all pixels in a local window (i.e., square) centered on the test pixel but excluding pixels inside a smaller inner square, provides an estimation of the background spectrum for the specific pixel. This is effective if a maximum target object size is known (to determine the radius of the inner square) and a minimum distance between target objects (to determine the radius of the outer square). There are other spatial factors that affect the effectiveness of local methods; in our test image, when looking for the vehicle targets, we are using a painted metal target spectrum and the background around the vehicle is likely to be road surface. There are likely other painted metal objects, such as roofs and other vehicles, that would not want to have a large impact on our background mean. Local statistics would be unlikely for a vehicle parked on a road surface near a metal-roofed building since the building spectrum would be similar to the target vehicle and not the road surface but the roof spectrum could be included in the local mean depending on window sizes. Local statistics have definite benefit when appropriate and can even provide a spatial filter on size, for example, detection of individual vehicles while excluding metal roofs. However, because spatial information about the size of target objects and distribution of target objects and other objects with similar spectra is not generally known, we will consider only global statistics in this paper.

For a given test pixel spectrum \mathbf{x} , the likelihood that the pixel belongs to a class with mean \mathbf{m} and covariance Σ is

$$L(\mathbf{m}, \Gamma; \mathbf{x}) = \frac{1}{\sqrt{(2\pi)^n |\Gamma|}} e^{-\frac{1}{2}(\mathbf{x}-\mathbf{m})^T \Gamma^{-1} (\mathbf{x}-\mathbf{m})}, \quad (2)$$

where n is the dimension of the data (number of bands).

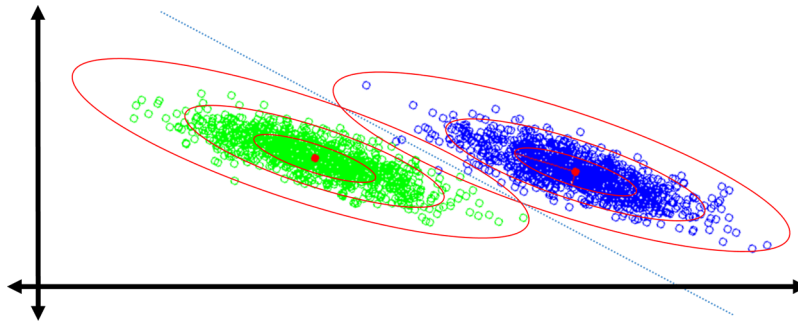


Fig. 1 Scatter plots of 1000 data points each from two multivariate normal distributions in two dimensions. For each distribution, we show the mean as a solid dot and the ellipses at MD^2 equal to 1, 4, and 12 units from the mean. The line of points that for have an equal likelihood for the two classes is shown as a dotted line.

Given a general classification problem to assign new data points to classes, each of which has a multivariate normal distribution, the method with the highest accuracy (i.e., the Bayes optimal method) is the Gaussian maximal likelihood classifier, which is just to assign each new data point to the class with the highest likelihood as computed in Eq. (2). A plot of two multivariate normal distributions is shown in Fig. 1. The quantity $MD^2 = (\mathbf{x} - \mathbf{m})^T \Gamma^{-1} (\mathbf{x} - \mathbf{m})$ in the exponent of Eq. (2) is a measure of the normalized distance to the class mean. The ellipses $MD^2 = 1, 4$, and 12 are shown for each distribution. Because the distribution of MD^2 is chi-squared with 2 degrees of freedom, the amount of data expected to be inside these ellipses is 39%, 87%, and 99.8%, respectively. The line of points that are equal likelihood for each class is shown as a dotted line. A maximum likelihood classifier would assign points above this line to the upper class, and points below to the lower class.

For the goal of detecting targets from background, this can be reduced to a single detection score by taking the ratio of the likelihoods, $L(\mathbf{t}, \Gamma; \mathbf{x}) / L(\mu, \Gamma; \mathbf{x})$. If this likelihood ratio is greater than one, the pixel is more likely to be target, and less than one is more likely to be background. More useful, however, is the log of the ratio of the likelihoods for the two classes, with the following equation

$$D(\mathbf{x}) = \log \left[\frac{L(\mathbf{t}, \Gamma; \mathbf{x})}{L(\mu, \Gamma; \mathbf{x})} \right].$$

This simplifies (canceling terms in the fraction and then using rules for exponents and logs) to

$$D(\mathbf{x}) = (\mathbf{x} - \mathbf{t})^T \Gamma^{-1} (\mathbf{x} - \mathbf{t}) - (\mathbf{x} - \mu)^T \Gamma^{-1} (\mathbf{x} - \mu). \quad (3)$$

If this log likelihood is greater than zero, the pixel is more likely to be target and less than zero is more likely to be background (given that the original assumptions are valid). For detection of a single target from background, there is a normalization that provides more convenient output values. Observe that the quadratic terms cancel in Eq. (3), leaving a linear operator $c \Gamma^{-1} (\mathbf{x} - \mu)$ (for some vector c). This linear operator is commonly scaled by a normalization constant to get the standard matched filter

$$MF(\mathbf{x}) = \frac{(\mathbf{t} - \mu)^T \Gamma^{-1} (\mathbf{x} - \mu)}{(\mathbf{t} - \mu)^T \Gamma^{-1} (\mathbf{t} - \mu)},$$

which has the property that $MF(\mu) = 0$ and $MF(\mathbf{t}) = 1$. Moreover, as we show in Sec. 3.1, the value of MF is the abundance of target if the test pixel is a linear mixture of target and background mean.

The maximal likelihood approach has an advantage over the likelihood ratio test in that it extends easily to a multiclass problem. Suppose we have N classes with means μ_n and

covariances Γ_n . Then we can use Bayes theorem (assuming that the test pixel is known to be in one of the provided classes) to show that the probability that a test pixel x belongs to class i is

$$P_i = \frac{L(\mu_i, \Gamma_i; \mathbf{x})}{\sum_{n=1}^N L(\mu_n, \Gamma_n; \mathbf{x})}.$$

This approach has advantages for material identification.^{9,10}

2.2 Covariance, Principle Components, and Whitening

In this section, we investigate the formulas underlying statistical target detection. This will be important in subsequent sections for investigating the underlying geometry.

For processing, it is common to write the image data as a matrix X whose i 'th column is the spectra \mathbf{x}_i of the i 'th pixel. (If there are k bands and N pixels, X is a $k \times N$ matrix.) The image data can be modeled with a probability distribution using a covariance matrix Γ [as in Eq. (2)] given by

$$\Gamma = \text{Cov}(X) = \frac{1}{N} \sum_{i=1}^N (\mathbf{x}_i - \mu)(\mathbf{x}_i - \mu)^T.$$

We can write the eigenvalue decomposition of Γ as

$$\Gamma = PDP^{-1},$$

where P is the matrix whose columns are the eigenvectors of Γ and $D = [\lambda_i]$ is the diagonal matrix whose elements are the corresponding eigenvalues ordered from largest to smallest. The matrix Γ is symmetric since each matrix $(\mathbf{x}_i - \mu)(\mathbf{x}_i - \mu)^T$ is symmetric, and so P is an orthogonal matrix ($P^{-1} = P^T$) and D is a diagonal real matrix. The inverse of Γ is therefore

$$\Gamma^{-1} = (PDP^{-1})^{-1} = PD^{-1}P^T = (P\sqrt{D^{-1}})(\sqrt{D^{-1}}P^T),$$

where $\sqrt{D^{-1}} = [\sqrt{1/\lambda_i}]$ since $D = [\lambda_i]$ is diagonal. (The matrix $\sqrt{D^{-1}}$ in our notation is the diagonal matrix whose i 'th diagonal element is $\sqrt{1/\lambda_i}$.)

The column vectors of $W = P\sqrt{D^{-1}}$ are called the “principle components” of the image. (Sometimes the column vectors of P , which are unit vectors in the same directions as the column vectors of W , are called the principle components.) Observe that

$$\Gamma^{-1} = (P\sqrt{D^{-1}})(\sqrt{D^{-1}}P^T) = (P\sqrt{D^{-1}})(P\sqrt{D^{-1}})^T = WW^T.$$

The principle components transform of the image is

$$Y = W^T(X - [\mu]),$$

where $[\mu]$ is the $k \times N$ matrix whose column vectors are μ . Application of the principle components transform is called principle components analysis. This transform, consisting of projection onto the (possibly scaled) eigenvectors of the covariance matrix, is also called the Karhunen–Loeve transform, Hotelling transform, or whitening transform. Whitening is a particularly descriptive term for our case since the covariance matrix of Y is the identity matrix—the column vectors of Y behave like white noise, as

$$\begin{aligned}
\text{Cov}(Y) &= \frac{1}{N} \sum_{i=1}^N (\mathbf{y}_i)(\mathbf{y}_i)^T \\
&= \frac{1}{N} \sum_{i=1}^N [W^T(\mathbf{x}_i - \mu)][W^T(\mathbf{x}_i - \mu)]^T \\
&= \frac{1}{N} \sum_{i=1}^N W^T(\mathbf{x}_i - \mu)(\mathbf{x}_i - \mu)^T W \\
&= W^T \left[\frac{1}{N} \sum_{i=1}^N (\mathbf{x}_i - \mu)(\mathbf{x}_i - \mu)^T \right] W \\
&= W^T \Gamma W \\
&= \left(P\sqrt{D^{-1}} \right)^T \left(P D P^{-1} \right) \left(P\sqrt{D^{-1}} \right) \\
&= \sqrt{D^{-1}} P^T P D P^{-1} P \sqrt{D^{-1}} \\
&= \sqrt{D^{-1}} D \sqrt{D^{-1}} = I.
\end{aligned}$$

The Mahalanobis distance of a pixel spectra is the value

$$\text{MD}(\mathbf{x}) = \sqrt{(\mathbf{x} - \mu)^T \Gamma^{-1} (\mathbf{x} - \mu)}.$$

The Mahalanobis distance is equal to the distance from x to the mean in whitened space,

$$\begin{aligned}
\text{MD}(\mathbf{x}) &= \sqrt{(\mathbf{x} - \mu)^T \Gamma^{-1} (\mathbf{x} - \mu)} \\
&= \sqrt{(\mathbf{x} - \mu)^T W W^T (\mathbf{x} - \mu)} \tag{4}
\end{aligned}$$

$$= \sqrt{[W^T(\mathbf{x} - \mu)]^T [W^T(\mathbf{x} - \mu)]} \tag{5}$$

$$= \|W^T(\mathbf{x} - \mu)\|. \tag{6}$$

The Mahalanobis distance of a spectra indicates how close the spectrum is to the class mean normalized by the variance of the class. A small Mahalanobis distance results in a high likelihood from Eq. (2). In the case in which Γ and μ are for a background class, the Mahalanobis distance gives a method for anomaly detection called the RX anomaly detection algorithm.¹¹ By the same computation, for any spectra \mathbf{a} and \mathbf{b} , we can compute the value obtained by whitening \mathbf{a} and \mathbf{b} and taking the dot product in whitened space using

$$(\mathbf{a} - \mu)^T \Gamma^{-1} (\mathbf{b} - \mu) = [W^T(\mathbf{a} - \mu)] \cdot [W^T(\mathbf{b} - \mu)]. \tag{7}$$

It is worth noting that MD^2 has a chi-squared distribution with degrees of freedom equal to the degrees of freedom of the data (possible the number of bands).

3 Target Detection Algorithms and Variants

In this section, we present the formulas and geometry of detection surfaces for a variety of target detection algorithms and variants. All of these detectors will be applied for our HyMap test data, with results presented in Sec. 4.

3.1 Mean-Centered (Covariance)-Based Detectors

Two of the most common target detection algorithms are the adaptive matched filter (AMF or just MF) and the adaptive coherence/cosine estimator (ACE). As described in Sec. 2.1, MF is the optimal detector assuming a multivariate normal background, and similarly ACE is the optimal

detector assuming a subpixel target and multivariate normal background. Their formulas are given by

$$D_{\text{AMF}}(\mathbf{x}) = \frac{(\mathbf{t} - \mu)^T \Gamma^{-1} (\mathbf{x} - \mu)}{(\mathbf{t} - \mu)^T \Gamma^{-1} (\mathbf{t} - \mu)}$$

and

$$D_{\text{ACE}}(\mathbf{x}) = \frac{(\mathbf{t} - \mu)^T \Gamma^{-1} (\mathbf{x} - \mu)}{\sqrt{(\mathbf{t} - \mu)^T \Gamma^{-1} (\mathbf{t} - \mu)} \sqrt{(\mathbf{x} - \mu)^T \Gamma^{-1} (\mathbf{x} - \mu)}},$$

where μ is the mean spectra from the image, \mathbf{t} is the target spectra, \mathbf{x} is the test pixel, and Γ is the covariance matrix. An additional detector worthy of note is Kelly's detector¹

$$D_{\text{Kelly}}(\mathbf{x}) = \frac{(\mathbf{t} - \mu)^T \Gamma^{-1} (\mathbf{x} - \mu)}{\sqrt{(\mathbf{t} - \mu)^T \Gamma^{-1} (\mathbf{t} - \mu)} \sqrt{\# \text{bands} + (\mathbf{x} - \mu)^T \Gamma^{-1} (\mathbf{x} - \mu)}}.$$

Both the MF and ACE have their derivations via signal processing and statistics. The assumption on MF is that the detection is that of a signal from Gaussian noise, and for ACE the assumption is that the signal is mixed according to the replacement model with Gaussian noise.

They can also be described by their geometry in whitened space as follows. For a spectra \mathbf{a} , we write the whitening transform of \mathbf{a} by $\hat{\mathbf{a}} = W^T (\mathbf{a} - \mu)$. By Eq. (7), we can rewrite MF and ACE as

$$D_{\text{AMF}}(\mathbf{x}) = \frac{\hat{\mathbf{t}}^T \hat{\mathbf{x}}}{\hat{\mathbf{t}}^T \hat{\mathbf{t}}}$$

and

$$D_{\text{ACE}}(\mathbf{x}) = \frac{\hat{\mathbf{t}}^T \hat{\mathbf{x}}}{\sqrt{\hat{\mathbf{t}}^T \hat{\mathbf{t}}} \sqrt{\hat{\mathbf{x}}^T \hat{\mathbf{x}}}}.$$

From basic vector algebra, the length of a vector \mathbf{a} is $\|\mathbf{a}\| = \sqrt{\mathbf{a} \cdot \mathbf{a}}$ and the scalar projection of \mathbf{a} onto a vector \mathbf{b} is $\mathbf{a} \cdot \mathbf{b} / \|\mathbf{b}\|$. Figure 2 shows a right triangle formed by $\hat{\mathbf{x}}$ and the projection of $\hat{\mathbf{x}}$ onto $\hat{\mathbf{t}}$, with an angle labeled θ . Observe that the lengths of the sides of the triangle are

$$\text{hypotenuse} = \sqrt{\hat{\mathbf{x}}^T \hat{\mathbf{x}}}, \quad (8)$$

$$\text{adjacent} = \frac{\hat{\mathbf{t}}^T \hat{\mathbf{x}}}{\sqrt{\hat{\mathbf{t}}^T \hat{\mathbf{t}}}},$$

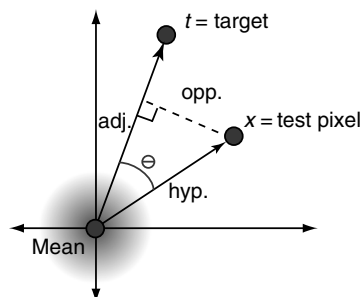


Fig. 2 Geometric relationships between the image mean spectrum, a test pixel spectrum, and a target spectrum. The quantities computed from these relationships are used in the MF, ACE, and F-test algorithms.

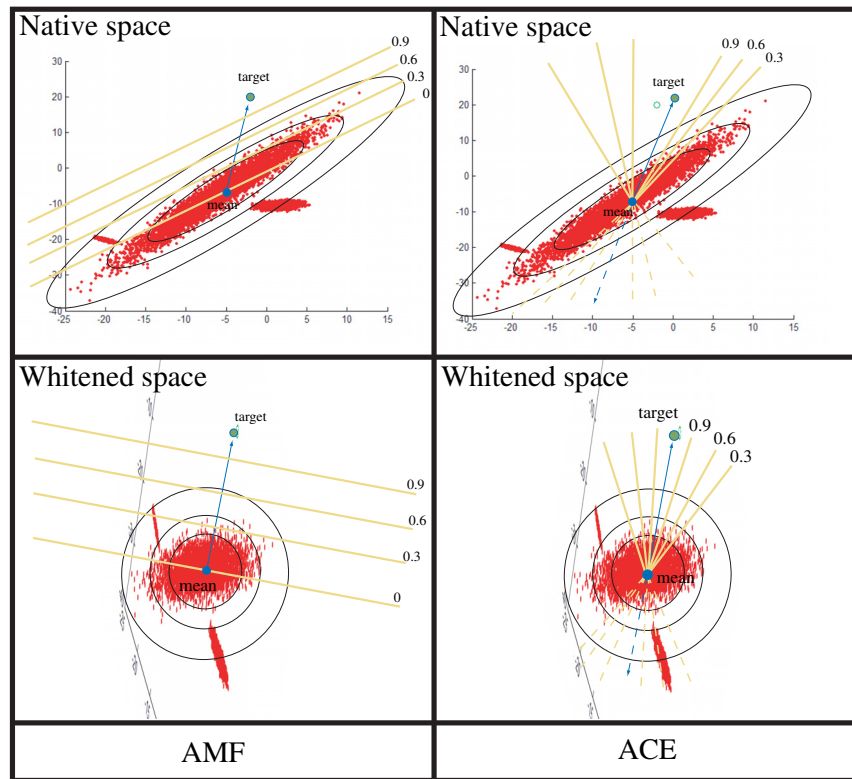


Fig. 3 A depiction of the decision surfaces for the MF and ACE algorithms using a synthetically generated data.

$$\text{opposite} = \sqrt{\text{hypotenuse}^2 - \text{adjacent}^2}.$$

From Eq. (8), we see that

$$D_{\text{MF}}(\mathbf{x}) = \frac{\text{adjacent}}{\|\hat{\mathbf{t}}\|}$$

and

$$D_{\text{ACE}}(\mathbf{x}) = \frac{\text{adjacent}}{\text{hypotenuse}} = \cos(\theta).$$

Observe that the adaptive matched filter is the scalar projection of $\hat{\mathbf{x}}$ onto $\hat{\mathbf{t}}$ normalized so that the MF score is equal to one when the projection is $\hat{\mathbf{t}}$. As depicted in Fig. 3, the decision surfaces for MF are hyperplanes and the decision surfaces for ACE are cones with vertex at the mean. A second version of ACE is sometimes given which is the square of the formula used in this paper. The decision surfaces for the $\cos^2(\theta)$ version are double cones since $\cos^2(\theta) = \cos^2(180 - \theta)$, shown in Fig. 3 as dashed lines.

3.1.1 *F*-test

An *F*-test is any statistical test in which the test statistic has an *F*-distribution under the null hypothesis. In hyperspectral imaging, it is used to determine a goodness of fit for a model of the pixel obtained from linear mixing of possible multiple target materials. The *F*-test has the form

$$F = \frac{\text{explained variance}}{\text{unexplained variance}}.$$

An F -test that is commonly used in hyperspectral imaging has the equation

$$D_{F\text{-test}}(\mathbf{x}) = (nb - 1) \frac{\text{MF}^2}{\hat{\mathbf{x}}^T \hat{\mathbf{x}} - \text{MF}^2},$$

where nb is the number of bands (degrees of freedom) in the image and MF is the adaptive matched filter. It is worth noting that if the pixel is being modeled as a linear mixture of k materials then the $(nb - 1)$ is replaced with $(nb - k)$. The real utility of the F -test for hyperspectral imaging is that it can be used to compare goodness of fit between two different models of a pixel with different numbers of materials. We show in the following that using the F -test as a detector is equivalent to using the ACE detector.

Observe that MF is the adjacent side of our triangle from Fig. 2 and that $\hat{\mathbf{x}} \cdot \hat{\mathbf{x}}$ is the hypotenuse squared. Thus, we have (using $\text{hyp}^2 - \text{adj}^2 = \text{opp}^2$ by the Pythagorean theorem)

$$D_{F\text{-test}}(\mathbf{x}) = (nb - 1) \frac{\text{adj}^2}{\text{hyp}^2 - \text{adj}^2} = (nb - 1) \frac{\text{adj}^2}{\text{opp}^2} = (nb - 1) \frac{1}{\tan^2(\theta)}.$$

Since $\tan^2(\theta)$ is monotonically increasing with θ and $\cos(\theta)$ is monotonically decreasing, the F -test and ACE give the same relative ranking for pixels. Thus, we will not consider the F -test further in this paper because its false alarm rates would be identical to ACE.

3.2 Nonmean-Centered (Correlation)-Based Detectors

The constrained energy minimization (CEM) algorithm (see Refs. 1 and 2) is similar to the MF except that the data are not mean-centered. It is also reasonable to evaluate a modification of ACE obtained by not mean centering, which we call ACE-NM.

$$D_{\text{CEM}}(\mathbf{x}) = \frac{\mathbf{t}^T \Sigma^{-1} \mathbf{x}}{\mathbf{t}^T \Sigma^{-1} \mathbf{t}}$$

and

$$D_{\text{ACE-NM}}(\mathbf{x}) = \frac{\mathbf{t}^T \Sigma^{-1} \mathbf{x}}{\sqrt{\mathbf{t}^T \Sigma^{-1} \mathbf{t} \sqrt{\mathbf{x}^T \Sigma^{-1} \mathbf{x}}}},$$

where Σ is the correlation matrix,

$$\Sigma = \text{Corr}(X) = \frac{1}{N} \sum_{i=1}^N \mathbf{x}_i^T \mathbf{x}_i.$$

As with the covariance based algorithms in Sec. 3.1, we can derive a triangle analogous to that shown in Fig. 2, except using nonmean-centered data and a correlation matrix. We would then obtain, similar to before, that

$$D_{\text{CEM}}(\mathbf{x}) = \frac{\text{adjacent}}{\|\hat{\mathbf{t}}\|}$$

and

$$D_{\text{ACE-NM}}(\mathbf{x}) = \frac{\text{adjacent}}{\text{hypotenuse}} = \cos(\theta).$$

3.3 Subspace-Projected Detectors

If μ is the image spectra mean then the matrix $P = I - \mu\mu^T$ is the projection onto the subspace orthogonal to the mean spectra. If X is the image matrix (# bands by # pixels) then PX will be

the projection of the image onto this subspace. The mean spectra of PX will be zero (in theory, ignoring computer rounding error which can impact the results). We can then define projected matched filter (PMF) and projected ACE (PACE) by

$$D_{\text{PMF}}(\mathbf{x}) = \frac{(P\mathbf{t})^T \Gamma^{-1} (P\mathbf{x})}{(P\mathbf{t})^T \Gamma^{-1} (P\mathbf{t})}$$

and

$$D_{\text{PACE}}(\mathbf{x}) = \frac{(P\mathbf{t})^T \Gamma^{-1} (P\mathbf{x})}{\sqrt{(P\mathbf{t})^T \Gamma^{-1} P\mathbf{t}} \sqrt{(P\mathbf{x})^T \Gamma^{-1} (P\mathbf{x})}},$$

where Γ is the correlation matrix

$$\Gamma = \text{Corr}(PX) = \frac{1}{N} \sum_{i=1}^N (P\mathbf{x}_i)(P\mathbf{x}_i)^T,$$

which is also the correlation matrix since the mean is zero.

It is also reasonable to consider the projected nonmean-centered ACE detector, which we refer to as PACENM.

It is also reasonable to attempt a simple approximation to removing illumination in an image projecting onto the unit vectors (equivalently scaling all spectra to have unit L1 norm). In our test, these algorithms are denoted by an *Il*- prefix, for example *Il*-MF is the matched filter applied after scaling all data to have unit L1 norm.

3.4 Infeasibility Detectors

The matched filter score measures the length of the projection of the mean-to-test-pixel vector onto the mean-to-target vector in whitened space as can be seen in Fig. 5. This is simply the length of the adjacent side of the triangle from Fig. 2. Pixels far from the mean-to-target vector score as high as pixels close to this vector if their projection has the same length. However, pixels close to this vector (i.e., close to the vertical axis in Fig. 5) are more target-like than pixels far from it. Thus, there have been efforts to use the distance from the mean-to-target vector, or some similar quantity, to measure “infeasibility” of a detection score. See Ref. 12.

For any constant ω , we define the infeasibility matched filter (IMF) by

$$\text{IMF}_{\omega}(\mathbf{x}) = \min[\text{MF}(\mathbf{x}), \omega \text{opp}(\mathbf{x})].$$

It is also reasonable to consider a projected infeasibility matched filter (PIMF).

3.5 Anomaly Removed Detectors

One fundamental challenge to the detectors discussed so far is that the data do not fit the assumptions for the derivation of the detectors. Specifically, the algorithms are derived assuming that the background (i.e., nontarget) portion of the image can be modeled with a normal probability distribution function. This PDF assumption is implicit in the use of covariance and correlation matrices.

The image data are complicated by the presence of “clutter” in the image — objects and materials that are anomalous other than the target. In fact, one can observe from the detections that many or most false alarms occur on clutter.

A second hindrance to detector performance is the presence of target materials in the covariance/correlation matrix. If targets are present in the image in sufficient quantities, the statistics will suppress the target in addition to the background.

For both of these reasons, it is common practice to test images using covariance/correlation matrices computed from subsets of the image chosen over homogeneous regions that are known to be free of targets (see Ref. 13). This process of computing statistics from more homogeneous target-free regions can be automated by applying an anomaly detection routine to the image and

computing the statistics from the nonanomalous regions of the image. We test both RX and the topological anomaly detector (TAD, see Refs. 14 and 15) for this purpose. One advantage to TAD is that it provides a percent background value that can be used to threshold the anomaly output to create a background mask. In our test image over Cooke City TAD estimated the background to be 97.8088%. In Ref. 15, TAD tested better than RX and several other anomaly detection algorithms.

3.6 Hybrid Combination Detectors

It has been observed that detector performance appears inconsistent; one detector may perform very well on one target but poorly on a different target, but combinations of detectors can improve accuracy in some cases (see Ref. 16.). In our test, ACENM had an exceptionally low number of false alarms on the Red Subaru target (10, in comparison to 2136 for ACE) but scored poorly on the subpixel red nylon (1140 false alarms for ACENM and 107 for ACE). While a complete discussion of hybridization is beyond the scope of this paper, we tested a very simple form of fusion without any rigorous or statistical method for identifying strengths of various detectors. After testing various combinations of detectors, we settled on the following hybrid detector:

$$\text{hybrid}(\mathbf{x}) = \max[\text{ACE}(\mathbf{x}), \text{ACENM}(\mathbf{x}), \text{PACE}(\mathbf{x}), \text{IMF}_2(\mathbf{x})].$$

These four detectors are so fundamentally different in structure and performance that they may improve results when combined. It would be very interesting to investigate rigorous fusion of algorithms with, for example, Dempster Schafer theory.

4 Results

Each algorithm in our test was tested with all six fabric targets and all three vehicle targets. For each detector–target pair, we computed the average false alarm rate, which is the average number of false alarms for the given target where the average is taken over all pixels that are on the given target. The results are presented in Tables 1 and 2. The first column contains the mean and standard deviation of the false alarm rates over all targets other than the green vehicle. The results are sorted by the mean average false alarm rate and are separated into two tables for display purposes.

The green vehicle seemed to be too difficult of a target for reliable algorithm evaluation, and the spread of values for this target would skew the results. Visual inspection of the pixel location for this target provided no indication of the presence of the target spectrum.

For a few of our detection algorithms, we include plots that show the data in whitened space with the target spectrum location. The plots for the ACE and MF detection algorithms are shown in Figs. 4 and 5, respectively. In each plot, the vertical axis is the projection of each pixel spectrum onto the target spectrum, and the horizontal axis is the distance from the mean in the subspace orthogonal to the target. That is, the vertical axis is the adjacent side and the horizontal axis is the opposite side from Eq. (8).

We plot the image data in this projection of “nonmean-centered-whitened” space in Figs. 6 and 7.

Plots showing the TAD-ACE detector results in “TAD-whitened” space are shown in Fig. 8 similar to Fig. 4 but using a covariance and whitening transform computed using TAD background pixels.

5 Discussion

In this section we provide conclusions from our tests, with general principles. First, we examine the general trends observable from the results in Tables 1 and 2. After that, we discuss limitations arising from imperfectly satisfied assumptions in the detector algorithms.

Table 1 Average false alarm rate for various detectors across all targets, for the better-scoring 32 algorithms. The first column is the mean value over all targets except the green vehicle. The green vehicle was deemed too difficult to provide reliable results.

Algorithm	Mean Std	RedC	YelN	BluC 2m 1m	RedN 2m 1m	(GrnV)	WhtV	RedV
(M) TAD-ACENM	633 0.41	80	50	310 470	10 1540	169,130	2510	90
II-RX-Kelly	650 -0.47	0	0	1 1168	37 420	6218	2605	967
(M) ACENM	653 -0.23	20	20	140 3420	10 1140	185,770	460	10
II-RX-ACE/SAM	660 -0.15	30	2	0 232	77 390	1153	2931	1617
II-TAD-ACE	674 -0.6	0	0	0 333	0 189	1321	2706	2163
II-TAD-Kelly	691 -0.49	0	0	3 1882	31 327	6247	1903	1380
II-TAD-ACE/SAM	695 -0.25	24	2	0 462	57 308	1063	2236	2473
II-Kelly	736 -0.49	1	0	4 1807	31 265	9504	3273	510
II-RX-ACE	821 -0.6	0	0	0 155	0 223	1391	5029	1160
II-ACE	1007 -0.6	0	0	0 286	0 174	2996	6939	654
TAD-ACE/SAM	1043 -0.29	23	0	0 608	47 221	625	6015	1430
P-TAD-ACE/SAM	1138 -0.02	27	0	0 1069	112 372	839	4968	2556
TAD*(TAD-ACE)	1183 -0.11	28	0	93 1567	51 257	1562	5810	1654
II-MF/SAM	1251 0.57	69	81	72 4974	145 1526	12,843	1911	1227
(M) TAD-MF	1332 -0.16	18	5	118 1323	41 315	2504	6596	2239
TAD-Kelly	1351 -0.59	0	0	0 682	0 147	1309	8690	1285
II-RX-MF	1369 0.46	61	60	182 4774	93 1418	12,068	2688	1676
II-RX-CEM	1369 0.46	61	60	182 4774	93 1418	12,068	2688	1676
(M) TAD-ACE	1434 -0.59	0	0	0 482	0 136	866	9866	986
II-TAD-MF	1446 0.73	52	104	388 5936	83 1328	12,267	1865	1815
II-TAD-CEM	1446 0.73	52	104	388 5936	83 1328	12,267	1865	1815
II-CEM	1453 0.33	55	33	189 5628	76 1187	16,263	3322	1131
TAD-MF	1510 -0.12	19	18	120 1374	42 325	2487	7776	2408
II-MF	1544 0.33	55	33	185 6000	78 1193	16,776	3709	1101
P-TAD-Kelly	1563 -0.58	0	0	0 710	0 147	1340	10,177	1472
TAD-CEM	1666 -0.1	19	23	123 1416	42 324	2520	8794	2586
P-TAD-MF	1673 -0.1	19	23	123 1413	42 324	2519	8842	2594
TAD-ACE	1720 -0.58	0	0	0 529	0 145	831	11,891	1196
(M) ACENM/SAM	1826 -0.06	20	20	210 11,770	20 1050	189,620	620	900
P-TAD-ACE	1993 -0.57	0	0	0 555	0 144	850	13,770	1472
(M) CEM	4843 -0.15	17	0	150 6640	0 120	202,400	22,590	9230
(M) IMF/SAM	5079 -0.12	23	16	34 3515	45 446	4330	33,479	3077

Table 2 Average false alarm rate for various detectors across all targets, for the lower scoring 32 algorithms. The first column is the mean value over all targets except the green vehicle. The green vehicle was deemed too difficult to provide reliable results.

Algorithm	Mean Std	RedC	YelN	BluC 2m 1m	RedN 2m 1m	(GrnV)	WhtV	RedV
MF/SAM	5081 -0.1	27	5	34 3528	47 454	4329	33,479	3077
(M) ACE/SAM	5856 0.01	39	10	0 3270	67 361	3380	41,027	2071
RX-ACE/SAM	5991 -0.01	34	0	0 301	74 277	431	45,813	1425
RX-MF	6014 0	24	44	51 852	54 411	2134	43,953	2719
P-MF/SAM	6219 0.31	31	19	49 6537	131 1994	4623	35,520	5471
RX-Kelly	6567 -0.47	0	0	0 336	0 193	1069	50,569	1438
(M) TAD-PACENM	6615 0.25	49	1	122 2756	64 6366	20,936	40,240	3323
RX-CEM	6644 0.04	24	54	53 900	54 417	2118	48,777	2869
ACE*TAD	6739 -0.17	22	0	29 3028	32 214	3909	49,357	1232
(M) PACE/SAM	7104 0.02	32	34	0 2316	62 332	3014	52,212	1841
RX-ACE	7313 -0.45	0	0	0 240	0 182	622	56,980	1102
“(M) IMF2	7663 -0.42	0	0	1 2174	4 168	6072	56,425	2529
(M) IMF	7686 -0.31	5	0	26 2193	16 196	6107	56,469	2584
(M) MF	7688 -0.25	12	0	26 2193	20 197	6107	56,470	2585
MF	7690 -0.25	12	0	26 2206	20 203	6106	56,469	2584
Kelly	7901 -0.42	0	0	0 1801	0 119	5307	59,525	1765
(M) ACE	8485 -0.42	0	0	0 2331	0 107	5463	63,306	2136
ACE	8487 -0.42	0	0	0 2344	0 114	5462	63,305	2135
(M) PACE	8493 -0.42	0	0	0 1693	0 117	4995	64,995	1138
P-CEM	9458 -0.19	14	0	29 2690	19 200	6516	69,275	3436
CEM	9578 -0.19	14	0	29 2682	19 198	6484	70,240	3441
P-MF	9696 -0.19	14	0	29 2739	19 200	6449	70,992	3578
P-Kelly	9827 -0.38	0	0	0 2477	0 120	5722	73,273	2743
P-ACE	10,338 -0.37	0	0	0 3494	0 114	6012	75,954	3138
(M) TAD-CEM	10,568 0.76	70	20	180 5840	0 140	179,810	3830	74,460
P-TAD-CEM	21,418 0.88	22	49	167 8606	72 1289	1717	10,8792	52,348
(M) PACENM	24,475 0.45	40	0	80 493	40 6570	18,690	187,510	1070
(M) PIMF/SAM	46,830 1.93	30	550	30 143,010	50 117,240	1840	113,110	620
(M) PMF/SAM	47,180 1.61	30	340	30 146,010	50 117,240	1910	113,110	630
(M) PIMF	51,629 1.07	20	0	40 135,850	30 123,290	4910	153,150	650
(M) PMF	51,633 1.09	20	10	40 135,850	30 123,290	4960	153,160	660
(M) TAD-PIMF	56,159 1.98	30	90	70 124,020	60 123,560	25,780	121,160	80,280

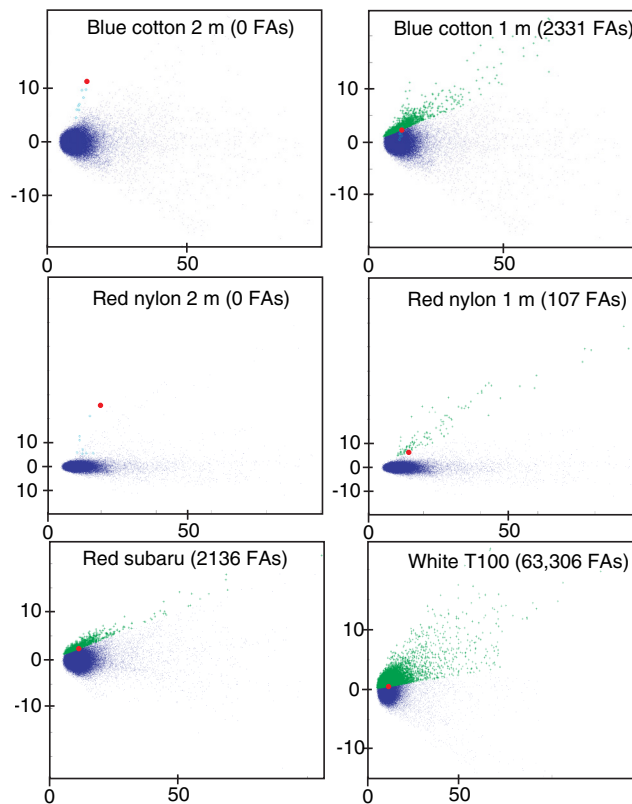


Fig. 4 Plots of the image data projected from whitened space with false alarms for ACE shown in green. The vertical axis is adjacent side and the horizontal axis is opposite side from Eq. (8). The highest scoring target pixel from the ground truth is shown in red. The false alarms—pixels scoring greater than the highest scoring target pixel from the ground truth—are shown in green. For the fabric panels additional ground truth target pixels are shown in teal. The number of false alarms is provided in the title for each plot.

5.1 Trends and General Guidelines

The full pixel fabric targets had a low range of average false alarm rates, while the vehicles were substantially higher. It is likely that an algorithm may perform very well overall but poorly on a single vehicle, and thus appear underperforming in our test. On the contrary, the algorithm with the lowest mean AFAR was (M) TAD-ACENM, which has poor false alarm rates on most targets but a low AFAR on the red vehicle, which ranks this algorithm higher than one would likely expect in general. Therefore, a direct comparison of algorithms based on a single number is probably not indicative of general difference in performance. It is more reliable to compare trends among classes of algorithms, or to compare algorithm scores on the whole, in a case-by-case manner.

The first notable trend from the results (Table 1) is that the best performing detectors tended to be quadratic detectors; the top 13 performing detectors were variations on ACE or Kelly. Illumination removal (or mean projection) and anomaly-removed statistics seemed generally effective.

From a practical perspective, a “best” algorithm is likely to be one that has excellent performance on the fabrics and preferably good performance on the vehicles. Accordingly, we reduced the number of detectors to produce Table 3, which includes only detectors that had zero false alarms on the 2-m fabric panels. All of these detection algorithms are quadratic detectors, a significant trend of improved performance of quadratic detectors over linear ones in our test (all our targets are subpixel, so this might be expected). With the best measured performance, both II-TAD-ACE and II-RX-ACE are top candidates. The top 10 detectors in this table are quadratic detectors with anomaly removal. After this top 10 group, the results drop off on

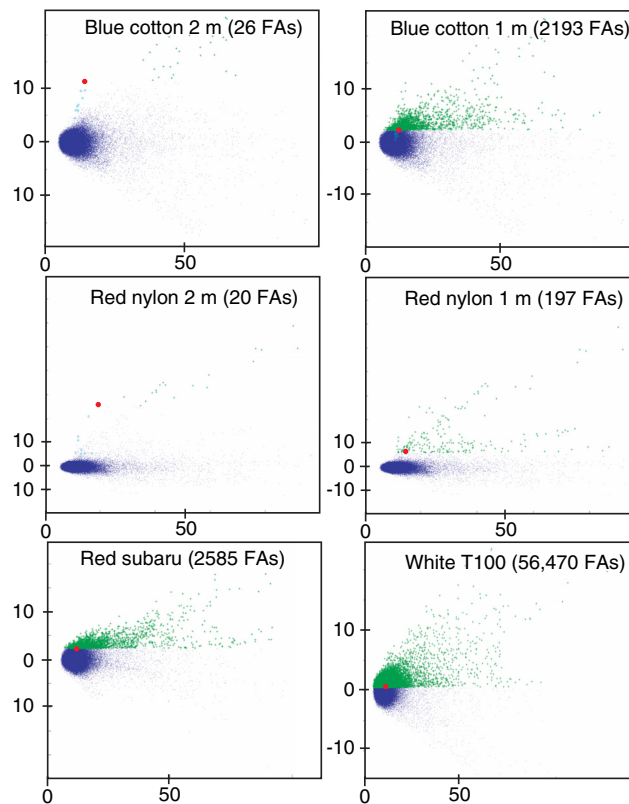


Fig. 5 Plots of the image data projected from whitened space with false alarms for MF shown in green. The vertical axis is adjacent side and the horizontal axis is opposite side from Eq. (8). The highest scoring target pixel from the ground truth is shown in red. The false alarms—pixels scoring greater than the highest scoring target pixel from the ground truth—are shown in green. For the fabric panels additional ground truth target pixels are shown in teal. The number of false alarms is provided in the title for each plot.

the 1-m blue cotton target and three vehicles; a significant trend that anomaly removal provides a robust improvement.

This illumination removal (or projection orthogonal to the mean) seemed effective in boosting performance particularly on the hard subpixel target; compare, for example, II-ACE to ACE (which is in Table 2). Illumination suppression seemed to help reduce the false alarm rate on the white vehicle, in particular, but not generally the other targets in Table 3. If a user prefers to not use a projection, both TAD-ACE and RX-ACE would be good performers under the above criteria; both of these had zero false alarms on the 2-m fabric panels, low false alarms on the small panels, but had a high false alarm rate on the white vehicle. They may be overpenalized in the test (if we were to use only the mean supplied in the first column) by performance on the white vehicle, particularly when we observe that TAD-ACE and RX-ACE scored well on the green vehicle that we removed from the mean computation in the first column.

Detectors that have a linear-shaped decision surface, such as matched filter, and detectors that have a quadratic-shape (or cone shape) such as ACE have different strengths and weaknesses that we can observe in their false alarms. Most algorithms perform quite well at separating the target spectra from the majority background material in the image, and most algorithms have a potential to false alarm on anomalous materials that have some similarity to the target. However, high reflectance pixels are a potential false alarm for linear detectors for reasons that are not present in quadratic detectors. As shown in Sec. 3.1, matched filter measures the length of the projection of a pixel onto the target (in mean-centered whitened space). Thus, a pixel with high intensity can have a large projection even if the direction of the spectrum vector is not toward the target. A pixel at location (10,30) in the plots of Fig. 3 would be one such pixel, with high intensity,

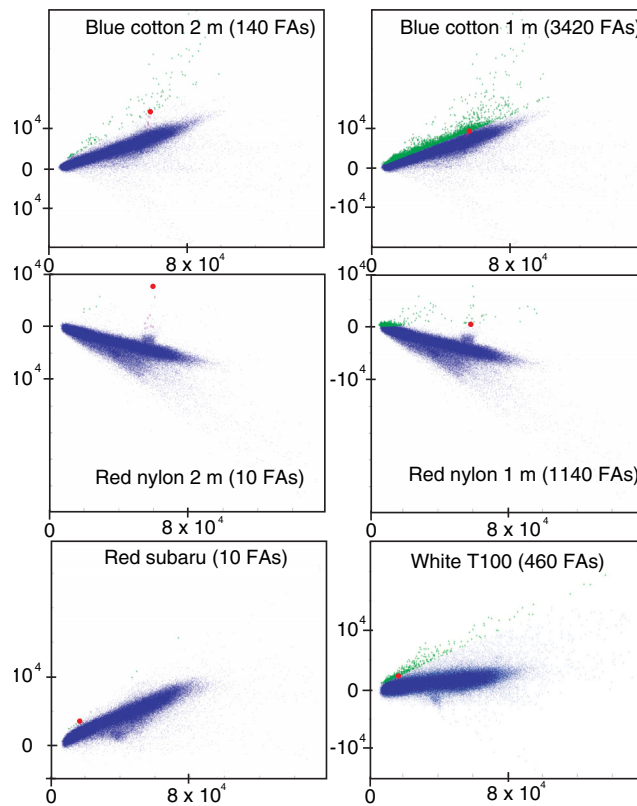


Fig. 6 Plots of the image data projected from “nonmean-centered whitened space” space with false alarms for ACE-NM shown in green. The vertical axis is adjacent side and the horizontal axis is opposite side from Eq. (8). The highest scoring target pixel from the ground truth is shown in red. The false alarms—pixels scoring greater than the highest scoring target pixel from the ground truth—are shown in green. For the fabric panels additional ground truth target pixels are shown in teal. The number of false alarms is provided in the title for each plot.

not particularly close to the target, and with a high MF score (greater than one, in fact) but a lower ACE score. The spectra in Fig. 9 include the red nylon lab-measured target spectrum, the pixel spectrum containing the target, and a false alarm (for MF) spectrum. The false alarm spectrum in this plot is a high-intensity MF false alarm; it has some features in common with the target (notice the shelf-shaped feature near 2250 nm indicating that both the false alarm and target are polymers), and some features that separate this spectrum from the target (shelf at 750 nm and upward slope from 750 to 1250 nm). However, being a bright pixel with intensity nearly twice that of the target spectrum, this is a false alarm for MF but not ACE; the ACE score for the nontarget pixel is 0.47 in comparison to 0.71 on the target pixel, while the MF score for this pixel is 0.27 in comparison to 0.13 on the target.

While there is no single best detection algorithm, we observed some significant trends. Overall, there was a consistent improvement in performance of quadratic algorithms in comparison to linear ones. Moreover, modifications such as anomaly removal, and to a lesser degree illumination normalization provided improvement in results. II-TAD-ACE and II-RX-ACE appeared to be top performers, and TAD-ACE and RX-ACE would be excellent choices if reflectance units (as opposed to illumination normalization) are preferred.

This conclusion is consistent with previous work, such as Ref. 17 where the conclusion was that ACE is robust, theoretically sound, and generally as good as any of the more complex algorithms available. In our investigation, we found that removing anomalies from computation of statistics provided significant robust improvement. This is a theoretically sound step, as it makes the covariance estimation more closely reflect the theoretical assumption that the covariance is for a single material class (the target or the background).

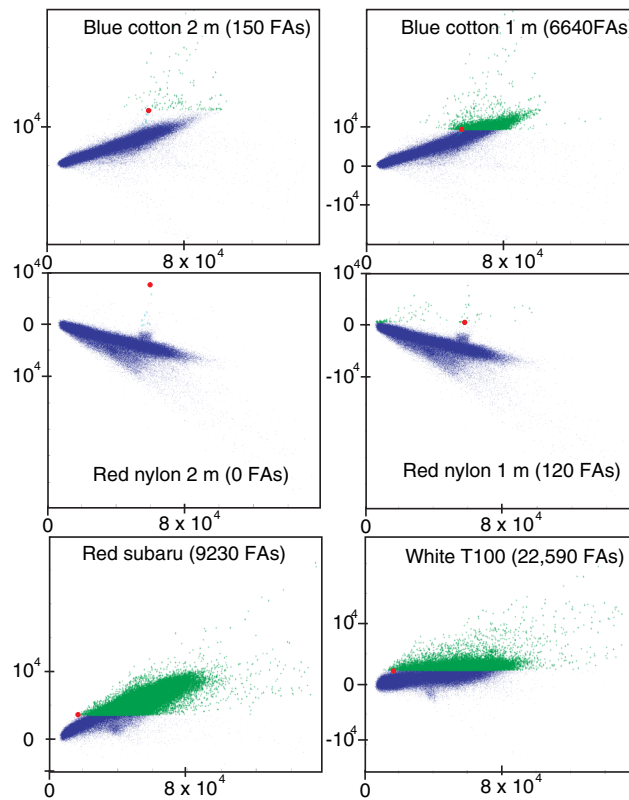


Fig. 7 Plots of the image data projected from “nonmean-centered whitened space” with false alarms for CEM shown in green. The vertical axis is adjacent side and the horizontal axis is opposite side from Eq. (8). The highest scoring target pixel from the ground truth is shown in red. The false alarms—pixels scoring greater than the highest scoring target pixel from the ground truth—are shown in green. For the fabric panels additional ground truth target pixels are shown in teal. The number of false alarms is provided in the title for each plot.

5.2 Effects of Imperfectly Satisfied Assumptions

As mentioned in Sec. 2.1, the assumption that the background is well-modeled by a multivariate normal distribution is known to not be generally satisfied in real hyperspectral images. It is reasonable to expect a single material class to be well-modeled by a multivariate normal distribution, but clearly images generally contain multiple background materials, resulting in a background that is at best a collection of mixtures of spectra from normal distributions. What may be more problematic than nonnormal multiclass backgrounds are rare nontarget materials in an image; rare material that is not similar to the target is called clutter, rare material that is not similar to the target is called clutter, and nontarget material with spectra similar to the target are called confusers. Both clutter and confusers can be detrimental to detection; either can impede proper covariance estimation of the background distribution and confusers are common causes of false alarms. In our test, the red polymer-painted roofs were confusers for the red nylon target, resulting in false alarms for the matched filter algorithm. Results from our test (and many other papers) show that hyperspectral imagery seems to be “normal enough” for good detection (granted this depends on individual requirements for “good enough” and the difficulty of detection for a given target), perhaps because the multivariate normal measures the subspace in which the data live, if not the true shape.

Figures 4–8 provide some insight into the effects of whitening from the multivariate assumption with a few variants. From Figs. 4 and 5, we see that the majority of the data is in a spherical cloud, as would be expected after whitening. We can also see the red nylon target is further from the mean in whitened space than the blue cotton targets; it seems that the red nylon is easier to detect with more “contrast” against this background. The linear and conic shape of the decision surfaces for MF and ACE can be observed in the false alarm pixels.

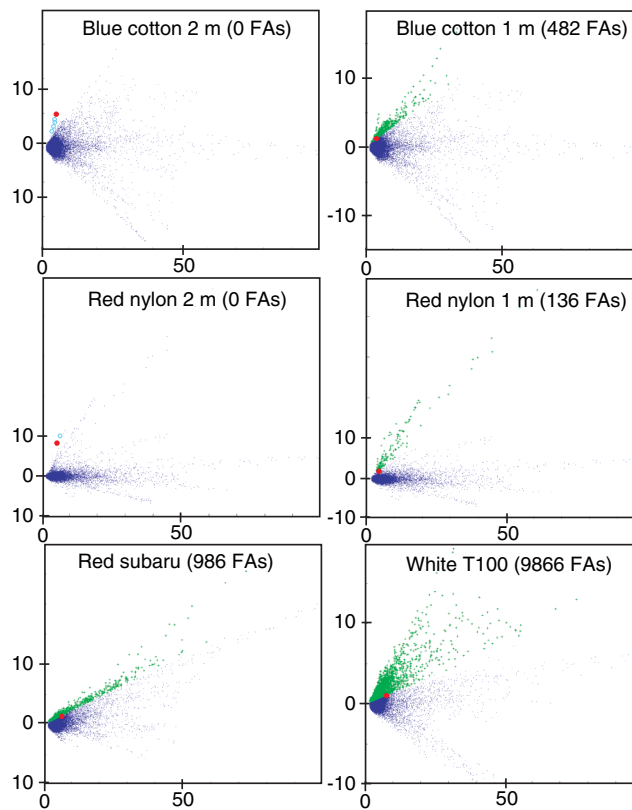


Fig. 8 Plots of the image data projected from whitened space with false alarms for TAD-ACE shown in green. The vertical axis is adjacent side and the horizontal axis is opposite side from Eq. (8). The highest scoring target pixel from the ground truth is shown in red. The false alarms—pixels scoring greater than the highest scoring target pixel from the ground truth—are shown in green. For the fabric panels additional ground truth target pixels are shown in teal. The number of false alarms is provided in the title for each plot.

From Figs. 6 and 7, we see the effects of whitening without subtracting the image mean spectrum. The data cloud is elongated, extending away from the origin in whitened space, as might be expected. Also, the data have more small observable structure. It is worth observing although ACE-NM had false alarms on the easy 2-m fabric targets, that the T100 and Red Subaru have contrast against the background when measured this way, and ACE-NM has a relatively low false alarm rate on these targets. It is an interesting question if there is a general principle in which ACE-NM is advantageous, perhaps involving the location of the vehicles on a road surface that is not common in the image at low abundance, or if these targets stand out from the background in this whitening method by chance in this test.

In Fig. 8, we observe the effects of anomaly removal in the statistics computation. The data cloud seems to have a tight sphere of data near the center, and linear structure extending radially outward. Presumably the linear structures correspond to anomalous material (roads, various roofs, etc.) in the image, and the main background classes (trees, grass, soil) form the tight sphere, being inherently closer to a multivariate normal distribution. It seems, from these plots and the low false alarm rates from anomaly-removed statics methods in our test, that the whitening allows measurement of the target mixed with background, while the angle-measurement in ACE enables discrimination between the target and other materials in the image.

There are a number of methods for building detection algorithms using a background model that does not assume normality. An excellent exposition of such methods is given in Ref. 18, where the conclusion is that there are methods for improving detection performance with better non-normal background models, but such methods are not necessarily robust and are not readily adaptable for non-experts in the respective fields of origin.

Table 3 Average false alarm rate across all targets but only for detectors that had a zero false alarm rates for the 2-m fabric panels. The first column is the mean value over all targets except the green vehicle. The green vehicle was deemed too difficult to provide reliable results.

Algorithm	Mean Std	RedC	YelN	BluC 2m 1m	RedN 2m 1m	(GrnV)	WhtV	RedV
II-TAD-ACE	674 -0.6	0	0	0 333	0 189	1321	2706	2163
II-RX-ACE	821 -0.6	0	0	0 155	0 223	1391	5029	1160
II-ACE	1007 -0.6	0	0	0 286	0 174	2996	6939	654
TAD-Kelly	1351 -0.59	0	0	0 682	0 147	1309	8690	1285
(M) TAD-ACE	1434 -0.59	0	0	0 482	0 136	866	9866	986
P-TAD-Kelly	1563 -0.58	0	0	0 710	0 147	1340	10,177	1472
TAD-ACE	1720 -0.58	0	0	0 529	0 145	831	11,891	1196
P-TAD-ACE	1993 -0.57	0	0	0 555	0 144	850	13,770	1472
RX-Kelly	6567 -0.47	0	0	0 336	0 193	1069	50,569	1438
RX-ACE	7313 -0.45	0	0	0 240	0 182	622	56,980	1102
Kelly	7901 -0.42	0	0	0 1801	0 119	5307	59,525	1765
(M) ACE	8485 -0.42	0	0	0 2331	0 107	5463	63,306	2136
ACE	8487 -0.42	0	0	0 2344	0 114	5462	63,305	2135
(M) PACE	8493 -0.42	0	0	0 1693	0 117	4995	64,995	1138
P-Kelly	9827 -0.38	0	0	0 2477	0 120	5722	73,273	2743
P-ACE	10,338 -0.37	0	0	0 3494	0 114	6012	75,954	3138

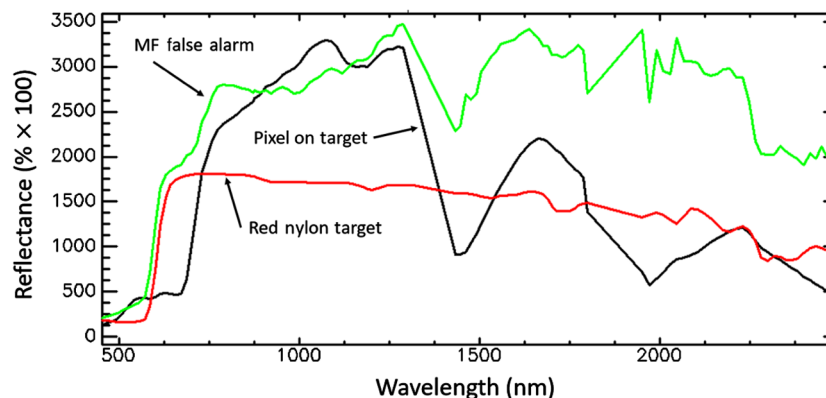


Fig. 9 Plots of the red nylon target (lab-measured) spectrum, a pixel on the 2 m target in the image, and a pixel that was scored higher than the target by MF are shown. The high-scoring pixel spectrum was a false alarm for MF but not ACE.

With regard to confusers, if spectra of confuser materials can be determined before collection, simply computing a detection score for the target and for confusers can aid in discriminating true targets from confusers.^{8,19} More robust methods, for example using a maximal likelihood or model averaging approach seem to be more effective.^{9,10} These methods, involving a detection stage to detect targets followed by an identification stage to separate targets from confusers, are very effective if confuser spectra can be determined before collection but are only as effective as

the confuser spectral libraries. They are not included in our test, because we are focusing on the detection stage alone, but are important to be aware of because they mitigate some not completely satisfied assumptions in our algorithms, and may be needed if robust detection is desired in a practical ongoing system.

6 Conclusions

In this paper, we tested a number of target detection algorithms and variants for hyperspectral imagery, and provided an analysis of the test results, the geometry of the different components of the detection algorithms, and the effects of the assumptions on the results. We found that the best detection algorithms were quadratic detectors with some modification to compute statistics that better satisfied the assumptions of the algorithm.

The modification that had a consistent improvement, across target types and quadratic detector variants, was anomaly removal prior to computing statistics. Removing anomalies results in a mean that is closer to the expected background of the image and different from target or clutter present in the image. Removing anomalies results in a covariance that more closely represents a covariance of a single material, which is an assumption for both the target and background variation in the algorithm derivation. In the whitened space scatter plots, we see that anomaly removal results in a tighter background, but also structures extending out from that background.

We also saw the effects of subtracting a mean (covariance) and not subtracting a mean (correlation) in detectors. Subtracting a mean seemed more effective in detecting targets mixed with a background similar to the image mean (fabric targets, in our test) whereas not subtracting a mean seemed more effective on targets that were mixed with a local background different from the image mean (vehicles, located on road surfaces, in our test). We did not have sufficient justification to say that this is a general principle, but does illustrate some of the strengths and weaknesses of the algorithms.

More than determining a single “best” target detection algorithm, we provided some insights into the personalities of different algorithms and modifications. We saw the importance of computing appropriate background statistics (both mean and covariance). We also provided ways to examine algorithms, for example the whitened space scatter plots, that can provide insight. We expect that this will be useful for future research, choosing or customizing algorithms for different purposes.

Acknowledgments

The authors are pleased to thank Marty Flynn for encouraging conversations on this work.

References

1. D. Manolakis, D. Marden, and G. Shaw, “Target detection algorithms for hyperspectral imaging application,” *Lincoln Lab. J.* **14**(1), 79116 (2003).
2. J. Schott, *Remote Sensing: the Imaging Chain Approach*, 2nd ed., Oxford University Press (2007).
3. J. Kerekes, “Target detection blind test,” <http://dirsapps.cis.rit.edu/blindtest/>.
4. D. Snyder et al., “Development of a web-based application to evaluate target finding algorithms,” in *IEEE Int. Geoscience and Remote Sensing Symp. (IGARSS '08)*, Vol. 2 (2008).
5. J. Harsanyi and C. Chang, “Hyperspectral image classification and dimension reduction: an orthogonal subspace project approach,” *IEEE Trans. Geosci. Remote Sens.* **32**(4), 779–785 (1994).
6. D. Gillis, P. J. Palmadesso, and J. H. Bowles, “Automatic target-recognition system for hyperspectral imagery using orasis,” *Proc. SPIE* **4381**, 34–43 (2001).
7. D. Manolakis, C. Siracusa, and G. Shaw, “Hyperspectral subpixel target detection using the linear mixing model,” *IEEE Trans. Geosci. Remote Sens.* **39**(7), 1392–1409 (2001).

8. W. Basener, "An automated method for identification and ranking of hyperspectral target detections," *Proc. SPIE* **8048**, 80480D (2011).
9. M. Halper and W. Basener, "Probabilistic identification of solid materials in hyperspectral imagery," US Patent App. 13/728, 501 (2014).
10. W. Basener, "Ensemble learning and model averaging for material identification in hyperspectral imagery," to be presented at *Algorithms and Technologies for Multispectral, Hyperspectral, and Ultraspectral Imagery XXIII, Defense and Commercial Sensing*, Paper 10198-56, SPIE, Anaheim, California (9–13 April 2017).
11. I. Reed and X. Yu, "Adaptive multiple-band CFAR detection of optical pattern with unknown spectral distribution," *IEEE Trans. Acoust. Speech Signal Process.* **38**, 1760–1770 (1990).
12. E. J. Ientilucci and J. R. Schott, "Physics based target detection using a hybrid algorithm with an infeasibility metric," in *IEEE Int. Conf. on Acoustics Speech and Signal Processing Proc.*, Vol. 5, pp. V–V (2006).
13. W. Basener, "Clutter and anomaly removal for enhanced target detection," *Proc. SPIE* **7695**, 769525 (2010).
14. B. Basener, E. J. Ientilucci, and D. W. Messinger, "Anomaly detection using topology," *Proc. SPIE* **6565**, 65650J (2007).
15. W. Basener and D. Messinger, "Enhanced detection and visualization of anomalies," *Proc. SPIE* **7334**, 73341Q (2009).
16. D. C. Grimm et al., "Hybridization of hyperspectral imaging target detection algorithm chains," *Proc. SPIE* **5806**, 753 (2005).
17. D. Manolakis et al., "Is there a best hyperspectral detection algorithm?" *Proc. SPIE* **7334**, 733402 (2009).
18. S. Matteoli, M. Diani, and J. Theiler, "An overview of background modeling for detection of targets and anomalies in hyperspectral remotely sensed imagery," *IEEE J. Sel. Top. Appl. Earth Obs. Remote Sens.* **7**(6), 2317–2336 (2014).
19. E. N. W. Basener and J. Kerekes, "The target implant method for predicting target difficulty and detector performance in hyperspectral imagery," *Proc. SPIE* **8048**, 80481H (2011).

William F. Basener is a research mathematician at Spectral Solutions, which he founded in 2006. He was professor at Rochester Institute of Technology in the School of Mathematical Sciences from 2000–2013, where he maintains an emeritus professor ranking, and is faculty at the University of Virginia in the Department of Systems and Information Engineering. His research areas include machine learning, data mining, applied topology, Bayesian statistics, and dynamical systems, with applications in remote sensing, population modeling, and genetics.

Biographies for the other authors are not available.